九州大学学術情報リポジトリ
Kyushu University Institutional Repository

Wavelet-based local region-of-interest reconstruction for synchrotron radiation X-ray microtomography

Li, Lingqi
Department of Production Systems Engineering, Toyohashi University of Technology

Toda, Hiroyuki
Department of Production Systems Engineering, Toyohashi University of Technology

Ogaki, Tomomi
Department of Production Systems Engineering, Toyohashi University of Technology

Kobayashi, Masakazu
Department of Production Systems Engineering, Toyohashi University of Technology

他

https://hdl.handle.net/2324/1807819

出版情報：Journal of Applied Physics. 102 (11), pp.114908-, 2007-12-01. American Institute of Physics
バージョン：
権利関係：

KYUSHU UNIVERSITY

Wavelet-based local region-of-interest reconstruction for synchrotron radiation X-ray microtomography

Lingqi Li, Hiroyuki Toda, Tomomi Ohgaki, Masakazu Kobayashi, and Toshiro Kobayashi

Department of Production Systems Engineering, Toyohashi University of Technology

Toyohashi, Aichi 441-8580, Japan

Kentaro Uesugi and Yoshio Suzuki

Japan Synchrotron Radiation Research Institute, Sayo-gun, Hyougo 679-5198, Japan

Abstract:

Synchrotron radiation X-ray microtomography is becoming a uniquely powerful method to non-destructively access three-dimensional internal microstructure in biological and engineering materials, with a resolution of 1-micrometer or less. The tiny field of view of the detector, however, requires that the sample has to be strictly small, which would limit the practical applications of the method such as in-situ experiments. In this paper, a wavelet-based local tomography algorithm is proposed to recover a small region of

interest inside a large object only using the local projections, which is motivated by the localization property of wavelet transform. Local tomography experiment for an Al-Cu alloy is carried out at SPring-8, the third-generation synchrotron radiation facility in Japan. The proposed method readily enables the high-resolution observation for a large specimen, by which the applicability of the current microtomography would be promoted to a large extent.

Keywords:

Local tomography, synchrotron radiation, wavelet transform, image analysis, aluminum alloy.

Ⅰ. INTRODUCTION

The computed tomography (CT) is a specialized imaging technique to measure the spatial distribution of the X-ray attenuation coefficients, which can reveal non-destructively the internal structure of an object and has been extensively used for medical diagnostic.[1] Currently, the third-generation synchrotron radiation (SR) facilities, such as SPring-8 in Japan, have been identified as ideal to CT, for the characteristics of high energy, high directionality, excellent lateral coherence and monochromaticity.[2] SR based microtomography (SR μ-CT) is becoming a uniquely powerful method to access

the internal microstructure in a metallic material, owing to its distinct advantages, such as three-dimensional (3D) visualization, non-destructive characterization, and high resolution observation with a spatial resolution of 1-micrometer or less.[3,4] Presently, SR μ-CT has been successfully employed for the quantitative assessments for mechanical properties of aluminum foams,[5-8] fatigue crack behavior,[9-12] and 3D high-density stain mapping.[13,14] As might have been expected, SR μ-CT will demonstrate itself to enable more promising applications to the material science and engineering.

In practical experiment, however, SR μ-CT suffers severely from the problem of limited field of view (FOV), mainly due to the limited element number of currently available detectors. For example, the FOV is nearly about 0.6-1.4 mm in width for a high-resolution projection-type SR μ-CT, and 50-100 μm in width for an ultra high-resolution imaging CT. It implies that the achievable resolution is inversely proportional to the sample diameter. In high-resolution observation, the sample has to be strictly small enough to fit the tiny FOV of the detector, which greatly limits the practical applications of the method such as in-situ experiments. This problem derives from the fact that the CT scan can be described mathematically by Radon transform (RT), whereas the inverse RT, i.e. the CT reconstruction, is not local in dimension two and in fact in any even dimension.[15] It means that the recovery of any fixed point at a

2D slice image requires the knowledge of all projections of this slice, not just the local portion passing though that point. If only a local portion of the projections is employed, the reconstructed image will be distorted in both the approximation and the singularities due to the aliasing, artifacts and noises arisen from the missed projections. Thus, developing an algorithm to enable the reconstruction of a local region of interest (ROI) inside a large sample has been of great interest recently.[16,17]

The local ROI reconstruction problem is also called local tomography, or interior Radon transform. The majority of the research on local tomography is contributed to medical diagnostic field, in order to reduce the radiation dose to patients. The existent algorithms can be categorized broadly into three categories: (1) iterative reconstruction method,[15,18] (2) pseudo-local tomography and lambda tomography,[19,20] and (3) modified filtered back projection (FBP) methods.[21-24] The principle of the iterative method is to minimize the I-divergency, or to maximize the statistical likelihood, so that an approximation of the local ROI can be achieved. Although conceptually this approach is simpler than transform-based methods such as FBP, it lacks the accuracy and suffers from the tough computation. Pseudo-local tomography uses local projections to determine the location and value of a discontinuity between a first internal density of an object and a second density of a region within the object.[19]

Lambda tomography maybe the method employed most popularly in medical field. However, same as the pseudo-local tomography, it is not a density function but a gradient-like function $\Lambda f + \alpha\Lambda^{-1} f$ that is reconstructed.[20] Both approaches are well adapted for edge detection only. In the FBP-based local reconstructions, various convolution kenels are constructed to modify the conventional FBP algorithm. Gabor expansion to the Radon transform was applied to give an inversion formula based on Gabor transform kenel.[21] Direct reconstruction of $\Delta^{1/2} f$ is performed with noise reduction. Some extension scheme for local sinogram to be pseudo-global was proposed, followed with the use of their modified FBP reconstruction, so that the local ROI of a patient can be obtained.[22] However, the low radiation dose to the structures outside the ROI at some sparse angles has to be sampled meanwhile. The non-locality of the 2D inverse RT still keeps unsolved. Most recently, a novel backprojection-filtration (BPF) algorithm was developed, in which it performs the data backprojection followed by the filtration of the backprojection. [23,24] This alternative BPF algorithm can achieve exact ROI reconstruction from truncated fan-beam data. It also provides a promising extension to the parallel-beam data, because the parallel-beam scan can be interpreted as a special case of the fan-beam scan by letting the focal length tend to infinity.

In this paper, the localization property of wavelet transform (WT) is

investigated. A wavelet-based ROI reconstruction algorithm is developed, and then applied to local ROI observation for an aluminum alloy by SR μ-CT scan. In the last decades, WT attracts more interest in the field of signal/image processing.[25,26] There have been a number of attempts using WT to local ROI reconstruction.[27-29] Unfortunately, these techniques still need to capture the global projections at some sparse angles to obtain a rough estimation of the global properties of the RT, which is difficult to implement in hardware for SR μ-CT imaging. Also, the irregular or interlace sampling scheme to the tomographic data consequently degrades the resolution of the reconstructed image, even though it succeeds in reducing the radiation dose or accelerating the reconstruction speed. For high-resolution metal microstructure analysis based on SR μ-CT scan, such research is not found yet in current literatures. The difference of the proposed algorithm from the others mentioned above is outlined as below. First, only local projections are used. No extra sparse sampling of the full exposure is needed, which will greatly facilitate the experimental implementation. Also, for high-resolution reconstruction, complete tomography data are employed, rather than downsampling or interlacing the sinogram. One approximation image and three other detail images in horizontal, vertical and diagonal orientations are reconstructed, respectively, which are used for inverse WT of the ROI image. What's more, a special

scheme for local sinogram extrapolation is also presented by which the reconstruction artifact and bias can be alleviated greatly.

The rest of this paper is organized as follows. Section Ⅱ briefly reviews the global and local tomography techniques, together with the inverse RT and its conventional FBP reconstruction method. The non-locality of FBP-based local tomography is also discussed. Section Ⅲ presents the local wavelet inversion of RT and the simulation results. Applications to SR μ-CT local ROI reconstruction, and some related discussion can be found in Section Ⅳ. The conclusion is summarized in Section Ⅴ.

Ⅱ. GLOBAL AND LOCAL TOMOGRAPHY Ⅱ

In SR μ-CT, the specimen is rotated and scanned by a SR X-ray beam, whose energy loss is recorded by a high-resolution CCD camera. Global tomography means that the sample should be enveloped completely by the X-ray, while the transmitted projection should be enclosed and captured within the FOV of CCD detector. Otherwise, it is called local tomography, as showed in Figure 1. The energy loss is regarded as the averages of the sample density function over lines, and can be described mathematically by the Radon transform.[1] The transmitted projections obtained on each scan angle

within π can assemble the sinogram which is used to reconstruct the corresponding slice image. In this study, only the 2D RT is considered for simplicity.

A. Radon transform and its inversion problem

Given a 2D function $f(\vec{x}),\ \vec{x}\in R^2$, its RT is defined by

$$Rf(\theta,s)=R_\theta f(s)=\int_{\theta^\perp} f\left(s\vec{\theta}+y\right)dy, \tag{1}$$

where $\vec{\theta}=(\omega_1,\omega_2),\ \omega_1^2+\omega_2^2=1,\ \theta\in[0,2\pi),\ s\in R$, and $\theta^\perp$ is the line perpendicular to $\vec{\theta}$. $Rf(\theta,s)$ represents the integral of $f(\vec{x})$ on the line $\theta^\perp$, and a directed distance s from the rotation origin. It is easy to get that $R_\theta f(-s)=R_{-\theta}f(s)$. The basic reconstruction formula is as following,

$$f*R^{\#}(g_\theta)(\vec{x})=R^{\#}(R_\theta f*g_\theta)(\vec{x}). \tag{2}$$

where $R^{\#}$ is the back projection (BP) operator, defined as $R^{\#}g(\vec{x})=\int_0^{2\pi} g\left(\vec{\theta},\vec{x}\cdot\vec{\theta}\right)d\theta.$ If g_θ is determined so that $R^{\#}(g_\theta)$ approximates a δ–function, then an exact approximation of $f(\vec{x})$ can be obtained by simple convolution and backprojection.

The most fundamental inversion formula is based on the fact that the Fourier transform (FT) of the 1D $Rf(\theta,s)$ corresponding to the variable s is the FT of the 2D function $f(\vec{x})$ alone a special line passing through the origin. This property is known as *Fourier slice theorem*,[1] which can be stated as follows:

$$\widehat{R_\theta f}(\omega) = \hat{f}(\omega\theta),\ \omega \in \hat{R}. \tag{3}$$

where ^ stands for the FT operator. Rewriting the Eq. (2) in polar coordinates leads to the FBP inversion formula, which is the standard method for global CT reconstruction

$$f(\vec{x}) = \int_0^{\pi}\int_{-\infty}^{\infty} \widehat{R_\theta f}(\omega) e^{2\pi j(\vec{x}\cdot\vec{\theta})\omega} |\omega| d\omega d\theta. \tag{4}$$

Thus, the FT of the projections at enough scan angles could in principle be assembled into a complete description of the 2D FT of the image, and then simply inverted to deliver the function $f(\vec{x})$.

B. Non-locality of 2D inverse Radon transform

To validate the motivation of using wavelet transform to local tomography in the proposed algorithm, it is necessary to first explore the non-locality of the 2D inverse RT. Consider the inverse RT formula in Eq. (2) in a general condition that in dimension *n*. We rewrite the BP portion in the left as follows:

$$R^{\#}(g_\theta)(\vec{x}) = G(\vec{x}) = R^{\#}\left(\frac{1}{2} I^{1-n} R_\theta G\right)(\vec{x}) \tag{5}$$

where I^{1-n} is the *Riesz potential operator* in dimension *n*. Thus we can get $g_\theta = \frac{1}{2} I^{1-n} R_\theta G.$ By the definition of I^{1-n} and the *Fourier slice theorem*, g_θ should satisfy the following condition:

$$\widehat{g_\theta}(\omega) = \frac{1}{2}|\omega|^{n-1} \widehat{G}(\omega\theta). \tag{6}$$

To invert the RT from local measurements, both g_θ and G have to be compactly supported. Suppose that $g_\theta(t)$ were compactly supported. Then according to the Fourier time-frequency analysis theorem, $\widehat{g_\theta}(\omega)=\frac{1}{2}|\omega|^{n-1}\widehat{G}(\omega\theta)$ must cover the entire frequency domain. However, it is impossible if the dimension n is even, because $|\omega|^{n-1}$ has a discontinuity in its $(n-1)^{st}$ derivative at $\omega=0.$ It implies that the RT has non-locality in even dimensions. Therefore, inverse RT can not be accomplished by local projections in the 2D SR μ-CT. In other words, to recover the accurate information of $f(\vec{x})$ at a local ROI, all projections are required. Actually, if n is odd, the locality is preserved, and it is the principle for the 3D local tomography. Unfortunately, it requires integrals over full 2D hyperplanes which we are trying to avoid.

Ⅲ. WAVELT-BASED LOCAL TOMOGRAPHY ALGORITHM

A. Wavelet transform

For the reasons mentioned above in Section Ⅱ. B, we try to find a basis of functions which possess essentially compact support and several vanishing moments as well. The vanishing moments will ensure that the basis functions remain compactly supported even after the filtering, which will allow the local reconstruction from the local projections. Recently, the wavelet transform has attracted more interest by signal

and image processing.[25, 26] Wavelets are generally compactly supported, as smooth as possible with many vanishing moments. Therefore, the time-spatial localization property of wavelet transform motivates the proposed algorithm to build the basis of functions for local ROI reconstruction.

The WT decomposes the signal onto translations and dilations of the mother wavelet ψ. Given a 2D function $f(\vec{x}), \vec{x} \in R^2$ satisfying the square integrable constraint. Then its WT can be written as

$$W_\psi f(u,\vec{v}) = f * D_u \psi^\vee(\vec{v}) \tag{7}$$

where $\vec{v} \in R^2$. Throughout our algorithm, the 2D isotropic dilation operator D_u is adopted as $D_u\psi(\vec{x}) = u^{-1}\psi(\vec{x}/u)$, and $\psi^\vee(\vec{x}) = \psi(-\vec{x})$. It can be noted that $(D_u\psi)^\vee = D_u(\psi^\vee)$, and $(\hat{\psi})^\vee = \widehat{\psi^\vee}$. Thus, the WT can be calculate in the spatial domain by

$$W_\psi f(u,\vec{v}) = u^{-1}\int_{R^2} f(\vec{x})\psi(\vec{x}/u - \vec{v})\, d\vec{x}. \tag{8}$$

And the inverse WT can be defined by

$$f(\vec{x}) = \int_{R^2}\int_R u^{-4} W_\psi f(u,\vec{v})\psi(\vec{x}/u - \vec{v})\, du d\vec{v}. \tag{9}$$

In this paper, discrete wavelet transform (DWT) is adopted, in which *u* is set to 2.

B. Wavelet local inversion for Radon transform

In the standard FBP method based on *Fourier slice theorem*, reconstruction is

accomplished by connecting the 1D FT of projection and the 2D FT of the image. To the local reconstruction problem, the Fourier transform is substituted by wavelet transform in the proposed algorithm, attempting to connect the WT of the 1D projection with that of the 2D function. This connection is built based on the back projection operation.

Suppose that ψ is a wavelet with some vanishing moment. We define a family of 1D functions $\left\{\widehat{\lambda_\theta}(\omega):\theta\in[0,\pi)\right\}$ in frequency domain by

$$\widehat{\lambda_\theta}(\omega)=\frac{1}{2}|\omega|\hat{\psi}(\omega\theta_1)\hat{\psi}(\omega\theta_2) \tag{10}$$

where $\vec{\theta}=(\theta_1,\theta_2),\ \theta_1^2+\theta_2^2=1,\ \theta\in[0,\pi).$ According to the *Fourier slice theorem*, Eq. (10) can be rewritten as $\widehat{\lambda_\theta}(\omega)=\frac{1}{2}|\omega|\widehat{R_{\theta_1}\psi}(\omega)\widehat{R_{\theta_2}\psi}(\omega),$ so that $\lambda_\theta(t)=\frac{1}{2}I^{-1}|\omega|R_{\theta_1}\psi(t)R_{\theta_2}\psi(t).$ Hence we can get

$$\left(R^{\#}\lambda_\theta\right)(\vec{x})=\frac{1}{2}R^{\#}\left(I^{-1}|\omega|R_{\theta_1}\psi(x)R_{\theta_2}\psi(x)\right)=\psi^{\vee}(x_1)\psi^{\vee}(x_2). \tag{11}$$

Next, we construct a corresponding separable 2D wavelet basis as follow:

$$\Psi(\vec{x})=\psi(x_1)\psi(x_2) \tag{12}$$

Now, let us recall the Eq. (2). If g_θ is determined by a wavelet as λ_θ, we can find that $R_\theta f * g_\theta$ in the right side is just the 1D WT of the projection $R_\theta f$ at a fixed angle θ, while the right are the 2D WT coefficients, which can be calculated by backprojecting the 1D WTs of the projections at all angles. In the presented algorithm, the function λ_θ is called wavelet ramp filter.

Suppose that ψ and ϕ are the wavelet and scaling functions for a wavelet basis with some vanishing moment, respectively. By using the method mentioned above, one scaling ramp filter and three wavelet ramp filters are constructed as below:

$$\begin{aligned}
\widehat{\lambda}_{\theta\,s}(\omega) &= \frac{1}{2}|\omega|\hat{\phi}(\omega\cos\theta)\hat{\phi}(\omega\sin\theta),\\
\widehat{\lambda}^{1}_{\theta\,w}(\omega) &= \frac{1}{2}|\omega|\hat{\phi}(\omega\cos\theta)\hat{\psi}(\omega\sin\theta),\\
\widehat{\lambda}^{2}_{\theta\,w}(\omega) &= \frac{1}{2}|\omega|\hat{\psi}(\omega\cos\theta)\hat{\phi}(\omega\sin\theta),\\
\widehat{\lambda}^{3}_{\theta\,w}(\omega) &= \frac{1}{2}|\omega|\hat{\psi}(\omega\cos\theta)\hat{\psi}(\omega\sin\theta).
\end{aligned} \tag{13}$$

And the corresponding 2D separable wavelet and scaling basis can be constructed by

$$\begin{aligned}
\Phi(\vec{x}) &= \phi(x_1)\phi(x_2),\\
\Psi^{1}(\vec{x}) &= \phi(x_1)\psi(x_2),\\
\Psi^{2}(\vec{x}) &= \psi(x_1)\phi(x_2),\\
\Psi^{3}(\vec{x}) &= \psi(x_1)\psi(x_2).
\end{aligned} \tag{14}$$

which are used for inverse WT defined by Eq. (9).

In our algorithm, 2D bi-orthogonal wavelet *bior3.3* is used, which is developed by Daubechies.[26] One approximation image and three other detail images in horizontal, vertical and diagonal orientations are reconstructed, respectively, which are used for inverse wavelet transform of the ROI image. As discussed in Section Ⅱ.B, the inversion of the RT is not local in even dimensions because the *Reisz potential operator* I^{1-n} has no compact support. If ψ has vanishing moments so that $I^{1-n}\psi$ decay rapidly, the local inversion of RT can be realized. It is well known that any wavelet has at least one vanishing moment, which gives a nearly same locally compact support for wavelet and

scaling ramp filters. This implies that the WT coefficients of $f(\vec{x}), \vec{x} \in R^2$, can be recovered locally from the local projections.

C. Local sinogram extrapolation

In local reconstruction, the artifacts are commonly close to the boundaries of the ROI. To illustrate this, we consider a 256×256 pixels Shepp-Logan head phantom and its centered ROI of 32-pixel radius, as showed in Figure 2 (a) and (b), respectively. Figure 2 (c) gives the ROI by global FBP method. It is well known that FBP can provide the best reconstruction if the projections are globally captured. If only the projections corresponding to the ROI are preserved, severe artifacts and noise will arise in the local reconstruction, as showed in Figure 2 (d).

Another observation can also be found in Figure 2 (d), in which there is a bias difference between the reconstructed ROI and the corresponding region in the original image. It has been proved that the error in the interior Radon transform is not negligible because of the loss of the measurement outside the ROI.[15] However, this error can be alleviated to be negligible by normalizing the reconstructed ROI and removing the bias difference, as showed later in Figure 3.

Based on the above observations, the presented algorithm adopts an

extrapolation scheme for local projections to alleviate the artifact and eliminate the bias. The supplementary projections, in which its length is determined by the number of coefficients of the wavelet ramp filters, are set to be the same value as the boundary projection of the ROI. Suppose that the length of the local projections is l_p, while the number of the wavelet ramp filter coefficients is l_w. The length of the extrapolated pseudo-global sinogram can be decided as $\sqrt{2}(l_p+2l_w)$. After reconstruction, only the central region with the diameter of l_p is extracted.

Figure 3 gives the simulation results of local ROI reconstruction. A centered ROI with the radius of 32 pixels inside the 256×256 pixels Shepp-Logan head phantom was reconstructed using our local WT-based algorithm. One-level DWT was carried out, and the result is given in Figure 3 (a). Figure 3 (d) shows the FBP reconstruction for comparison. Figure 3 (b) and (e) are their residuals to the original ROI, respectively. It can be found that the proposed method can provide more accurate reconstruction of the local ROI, especially at the singularities, such as the boundaries. FBP method can not avoid these artifacts, even though the same extrapolation of local projections is taken.

To quantitatively evaluate the performance, the mean square error (MSE) between the original image and the locally reconstructed image was calculated and given in Figure 3. To highlight the differences, Figure 3 (c) and (f) illustrate the

magnified residuals. More noises arose in the FBP reconstructed ROI image. Apparently, our algorithm performs superior to the FBP, both in the visual interpretability and in quantitative MSE evaluation.

The presented wavelet-based local ROI reconstruction algorithm is summarized as follows:

- Construct the scaling and wavelet ramp filters;
- Extrapolation of local projections;
- Perform 1D DWT for each projection at each angle;
- Backproject the 1D WT coefficients to provide the WT coefficients of 2D $f(\vec{x})$;
- Perform 2D inverse DWT to reconstruct the $f(\vec{x})$.

In the implementation of wavelet filtering, we do not perform the down-sampling for the projection data. Full sampling provides higher resolution for the reconstructed image, despite lowering the reconstruction speed.

Ⅳ. APPLICATION TO MATERIALS IMAGING IN A SR μ-CT EXPERIMENT

A. Experimental setup

Local tomography experiments were carried out at the SR X-ray imaging

beamline BL20XU of the Japanese third-generation synchrotron radiation facility (SPring-8) in Japan. The photon energy of the monochromatic X-ray beam was set 30 kev using a double crystal monochromator. The specimen was an Al-4.4%Cu alloy. Tomographic scans were performed under a successive increment of equidistant angle during 180-degree rotation of the sample, and 1500 transmitted images were picked up by the CCD camera. The combination of the CCD detector (4000×2624 pixel, 2×2 binning mode, 5.9×5.9 μm^2 pixel size) and the optical lens provides an isotropic 0.474 μm^3 voxel. The FOV of this experimental setup is 0.948×0.622 mm^2. This demands that, for common global tomography, the specimen must be surrounded within the radiation diameter of 0.948 mm while being rotated.

In this experiment, the diameter of a cylinder specimen is 4.0mm. Figure 4 (a) gives the experimental setup at SPring-8, and (b) illustrates the schematic diagram of the specimen. Reconstruction results of the ROI images at the center of the specimen are reported in Figure 5. In Figure 5, (a) is reconstructed by wavelet-based local tomography algorithm, while (b) by the FBP method. Both images are 2000×2000 pixels. Two magnified images of 512×512 pixels, corresponding to the same region, are given by Figure 5 (c) and (d), respectively, aiming at performance comparison and evaluation.

B. Results and discussion

1. Image clarity and interpretability

Image clarity and interpretability of the reconstructed slice establish the foundation for feature detection and extraction, texture classification, and microstructure understanding. Obscure slice image will result in unreliable even false conclusion. By subjectively comparing the overall image clarity, it is notable that Figure 5 (c), by our method, is better than (d), by FBP reconstruction. The profiles of pores *A*, *B*, and particle *C* extracted from our reconstructions, as indicated in Figure 6, are clearer and easier to be recognized owing to their sharp edges. But in FBP reconstruction, the shapes of pore *A* and *B* are blurred severely, and some patterns are even missed, (e.g. pore *B*). This can also be demonstrated by the post feature segmentation, as given in Figure 5 (e) and (f). These phenomena come from the non-locality of FBP reconstruction. The artifact arisen in reconstruction corrupts the edge information. Besides, the particle Al_2Cu, the light white region, exhibits lack of contrast too, which will degrade the ability to obtain accurate quantitative investigation from the reconstructed images.

2. Signal-to-noise ratio

To evaluate the noise in the reconstructed images, signal-to-noise ratio (SNR) is calculated, which is defined as the ratio of the mean pixel value to the standard deviation of the pixel values. Eight regions were randomly picked up. Each one is 256×256 pixels, containing microstructures such as particles, or pores. Figure 7 gives the evaluation results. The SNRs of all the 8 regions from the reconstruction by the presented algorithm are lager than those by the FBP method.

3. Spatial resolution

Spatial resolution is one important criterion to evaluate a reconstruction technique for a SR μ-CT imaging system. The resolution can be referred to the blurring degree along the boundaries between dissimilar phases. For quantitatively evaluation, full width at half maximum (FWHM) is measured based on the edge spread function (ESF) and line spread function (LSF). The ESF indicates the 1D response to an ideal edge, while its first derivative is called LSF. The FWHM is just the span between the two points at the half maximum of LSF.

Due to the discontinuity of the pores density, the profile crossing it should be a step function by an ideal reconstruction. Therefore, the pore profiles are extracted to

measure the FWHM. For a practical edge profile from the reconstructed image, it can be regarded as a blurred and noised result of an ideal edge.

To calculate its LSF, the edge profile is first fitted to a sigmoid function by

$$f(x)=\frac{a}{1+e^{-(x-b)/c}}. \tag{15}$$

Two edge profiles of the pore *A* in Figure 7 are separately cut out and normalized. The average of these two corresponding FWHM values is utilized to evaluate the spatial resolution. Shorter FWHM indicates that the image has higher spatial resolution. Figure 8 reports the results. It is remarkable that the proposed method can achieve higher spatial resolution by 3 times that by standard FBP method.

Based on the above qualitative and quantitative evaluations of the reconstruction performance, it can be concluded that the proposed wavelet local tomography algorithm can provide an accurate and reliable solution to the limited FOV problem of SR μ-CT imaging. To check the relationship between the non-local size of the sample and the reconstructed image quality, three closed-cell aluminum foam specimen (Al-10.0%Zn-1.5%Ca-1.6% Ti-1.0%Mg) were scanned by the SR X-ray in SPring-8. Their diameters are 7mm, 14mm and 28mm, respectively. The reconstructed images are displayed in Figure 9. Even the size of the foam is 14 times larger than the FOV of the SR X-ray, our algorithm can deliver clear details of the foam cell and the

pores, as showed by Figure 9 (b). It should be noted that if the specimen is too large to permit the transmission of the X-ray, our method could not work well, as given by Figure 9 (c), where the diameter of specimen is about 30 times larger that the width of FOV. The transmitted images captured by CCD camera become black so that the projection information within them can be hardly recognized. Even though the proposed algorithm is independent of the non-local size, the obtained local projections must be informative enough. It is a fundamental constraint for practical local ROI reconstruction of SR μ-CT.

Ⅴ. CONCLUSION

The standard filtered back projection method can not provide the precise reconstruction of a cross slice of specimen, if it exceeds the field of view of the synchrotron radiation X-ray beam. This problem comes from the non-locality of 2D inverse Radon transform. In this paper, a wavelet-based local tomography algorithm is proposed, which can stably realize the accurate and reliable reconstruction for a region of interest inside a large sample. The presented algorithm is motivated by the time-spatial localization property of wavelet. The local reconstruction only uses the local projections corresponding to the region of interest. No extra sparse sampling for

the full exposure is needed, which greatly facilitate the experimental implementation in hardware. The local tomography experiments were carried out at SPring-8 in Japan. The experimental results demonstrate that the presented wavelet-based local tomography algorithm outperforms to the standard filtered back projection method, both on qualitative and on quantitative evaluations. Higher spatial resolution and higher signal-to-noise ratio of the reconstructed images can be achieved, which readily ensure the accurate and reliable post-processing, such as quantitative assessment of mechanical properties, 3D micro-feature extraction, phase recognition, and component segmentation. It should be pointed out that the transmitted projections should be recognizable with adequately valid information.

Synchrotron radiation X-ray microtomography had found more and more applications to the material science and engineering. The proposed wavelet-based local tomography algorithm can overcome the limited field of view problem, enabling the high-resolution observation of a large sample. Such enhancement would promote the applicability of the current microtomography to a large extent. It is reasonable to expect that zoom lens observation of an internal interest domain, like an optical microscope, could be realized in the nearest future.

ACKNWLEDGEMENT

This work is partially supported by the New Energy and Industrial Technology Development Organization (NEDO) of Japan. The authors thank for supporting by SPring-8/JASRI (Proposal No. 2006B1239 and 2006B1018), Aluminum Research Aid, TAREMATSU Foundation, and the Light Metal Educational Foundation. The authors also appreciate the anonymous reviewers for their thorough reading of this paper and their constructive comments.

References

[1.] A. C. Kak and M. Slaney, Principles of Computerized Tomographic Imaging, (Society of Industrial and Applied Mathematics, 2001).

[2.] J. Baruchel, J. Y. Buffiere, P. Cloetens, M. D. Michiel, E. Ferrie, W. Ludwig, E. Maire, and L**.** Salvo**,** Scri. Mater. **55**, 41 (2006).

[3.] K. Uesugi, Y. Suzuki, N. Yagi, A. Tsuchiyama, and T. Nakano, Nuclear Instruments and Methods in Physics Research Section A: Accelerators, Spectrometers, Detectors and Associated Equipment, **467,** Part 2: 853 (2001),

[4.] H. Toda, K. Uesugi, A. Takeuchi, K. Minami, M. Kobayashi, and T. Kobayashi, Appl. Phys. Lett. **89,** 143112 (2006).

[5.] H. Toda, H. Mizutani, T. Akahori, M. Niinomi, and T. Kobayashi**,** Mater. Trans. **46**, 2229 (2005).

[6.] H. Toda, T. Ohgaki, K. Uesugi, M. Kobayashi, N. Kuroda, T. Kobayashi, M. Niinomi, T. Akahori, K. Makii, and Y. Aruga, Metall. Mater. Trans. A. **37A** 1211 (2006).

[7.] H. Toda, J. Katano, T. Kobayashi, T. Akahori, and M.Niinomi, Mater. Trans. **46**, 111 (2005)

[8.] T. Ohgaki, H. Toda, I. Sinclair, J. Buffiere, W. Ludwig, T. Kobayashi, M. Niinomi, and T. Akahori, Mater. Sci. Eng. A, **406**, 261 (2005).

[9.] L. Qian, H. Toda, S. Nishido, and T. Kobayashi, Acta Mater. **54**, 4881 (2006).

[10.] E. Ferrie, J. Y. Buffiere, W. Ludwig, A. Gravoui, and L. Edwards, Acta Mater. **54**, 1111 (2006).

[11.] H. Toda, I. Sinclair, J. Y. Buffiere, E. Maire, K. Khor, P. Gregson, and T. Kobayashi, Acta Mater. **52**, 1305 (2004).

[12.] H. Toda, I. Sinclair, J. Y. Buffiere, E. Maire, T. Connolley, M. Joyce, K.H. Khor, and P. Gregson, Philos. Mag. **83**, 2429 (2003).

[13.] M. Kobayashi, H. Toda, T. Ohgaki, K. Uesugi, D. S. Wilkinson, T. Kobayashi, Y. Kawai, and Y. Aoki, Mater. Sci. Forum. **539-543**, 2377 (2007).

[14.] J. Ahn, H. Toda, M. Niinomi, T. Kobayashi, T. Akahori, and K. Uesugi, Review of progress in QNDE. **760**, 1423 (2005).

[15.] A. Ramm and A. I. Katsevich, The Radon Transform and Local Tomography, (Boca Raton: CRC Press, 1996).

[16.] T. Ohgaki, H. Toda, K. Uesugi, T. Kobayashi, K. Makii, T. Takagi, and Y. Aruga, Mater. Sci. Forum. **539-543**, 287 (2007).

[17.] A. Faridani, D. Finch, E. L. Ritman, and K. Smith, SIAM J. Appl. Math. **57**, 1095 (1997).

[18.] G. Wang, D. Snyder, and M. Vannier, Scanning. **18**, 582 (1996).

[19] A. Faridani, F. Keinert, F. Natterer, E. Ritman, and K. Smith, Signal processing part II: control theory and applications, (Springer-Verlag, NY, Inc. USA, , 1990) 241.

[20] A. I. Katsevich and A. G. Ramm, SIAM J. Appl. Math. **56**, 167 (1996).

[21] D. Walnut, Probabilistic and Stochastic Methods in Analysis, with Applications, J. Byrnes, et al. Eds. (Boston, MA: Kluwer, 1992) 187.

[22] H. Yu, Y. Ye, S. Zhao, and G. Wang, Int. J. Biomed. Imaging. **2006**, 1 (2006).

[23] X. Pan, Y, Zou, and D. Xia, Med. Phys. **32**, 673 (2005).

[24] Y, Zou, X. Pan, and E. Sidky, Phys. Med. Biol. **50**, 13 (2005).

[25] S. Mallat, IEEE Trans. Patt. Anal. Machine Intell. **11**, 674 (1989).

[26] I. Daubechies, Ten Lectures on Wavelets. (Philadelphia, PA: SIAM, 1992).

[27] T. Olson and J. DeStefano, IEEE Trans. Sig. Proc. **42**, 2055 (1994)

[28] F. Rashid-Farrokhi, R. Liu, C. Berenstein, and D. Walnut, IEEE Trans. on Image Proc. 6, 1412 (1997).

[29] C. Berenstein and D.Walnut, 75 Years of Radon Transform, S. Gindikin and P. Michor, Eds. (Cambridge, MA: Int. 1994) 38.

List of Figure Captions

FIG. 1. Schematic view of global and local tomography.

FIG. 2. (a) 256×256 pixels Shepp-Logan head phantom, (b) the centered region with radius of 32 pixels; (c) reconstruction by global projections, and (d) reconstruction by local projections.

FIG. 3. Simulation of local reconstruction for the centered region with radius of 32 pixels inside the 256×256 pixels Shepp-Logan head phantom. (a) and (d) are reconstructed by the proposed algorithm and the local FBP method, respectively, (b) and (e) are the corresponding residuals to the original centered region, with the MSE are 0.007 and 0.027, respectively, (c) and (f) are the highlighted residuals multiplied by 3.

FIG. 4. (a) Local tomography experimental setup at SPring-8 in Japan, and (b) the schematic diagram of the specimen.

FIG. 5. Reconstruction results of local tomography experiment at SPring-8. (a) by the

proposed algorithm, (b) by FBP method, both images are 2000×2000 pixels. (c) and (d) are two zoomed images of 512×512 pixels, corresponding to the same region, respectively, (e) and (f) are their feature extracting results.

FIG. 6. Profile checking: (a) and (c) are the reconstructed profiles by the proposed method, while (b) and (d) by FBP method. These four profiles are extracted from the two magnified images of 512×512 pixels in FIG. 5. Their locations are: (a) and (b) y = 207; (c) and (d) x = 214, respectively.

FIG. 7. SNR evaluation results, where the 8 regions are selected randomly in the reconstructed images.

FIG. 8. The FWHM measurements of reconstructed images: (a) and (b) are the sigmoid fitting for the downward and upward edges of pore A, by the proposed algorithm and FBP method, respectively; (c) and (d) are the measured FWHM of the proposed reconstruction, where the average FWHM is 6.4 pixels (3.03 μm); (e) and (f) are of FBP reconstruction, where the average FWHM is 19.1 pixels (9.05 μm).

FIG. 9. Reconstructions by the proposed algorithm for three closed-cell aluminum foam (Al-10.0%Zn-1.5%Ca-1.6%Ti-1.0%Mg) specimen with different diameters: (a) 7mm, (b) 14mm, and (c) 28mm. The FOV is 0.95 mm in width. (d), (e) and (f) are one piece of their corresponding transmitted projection images, respectively.

1

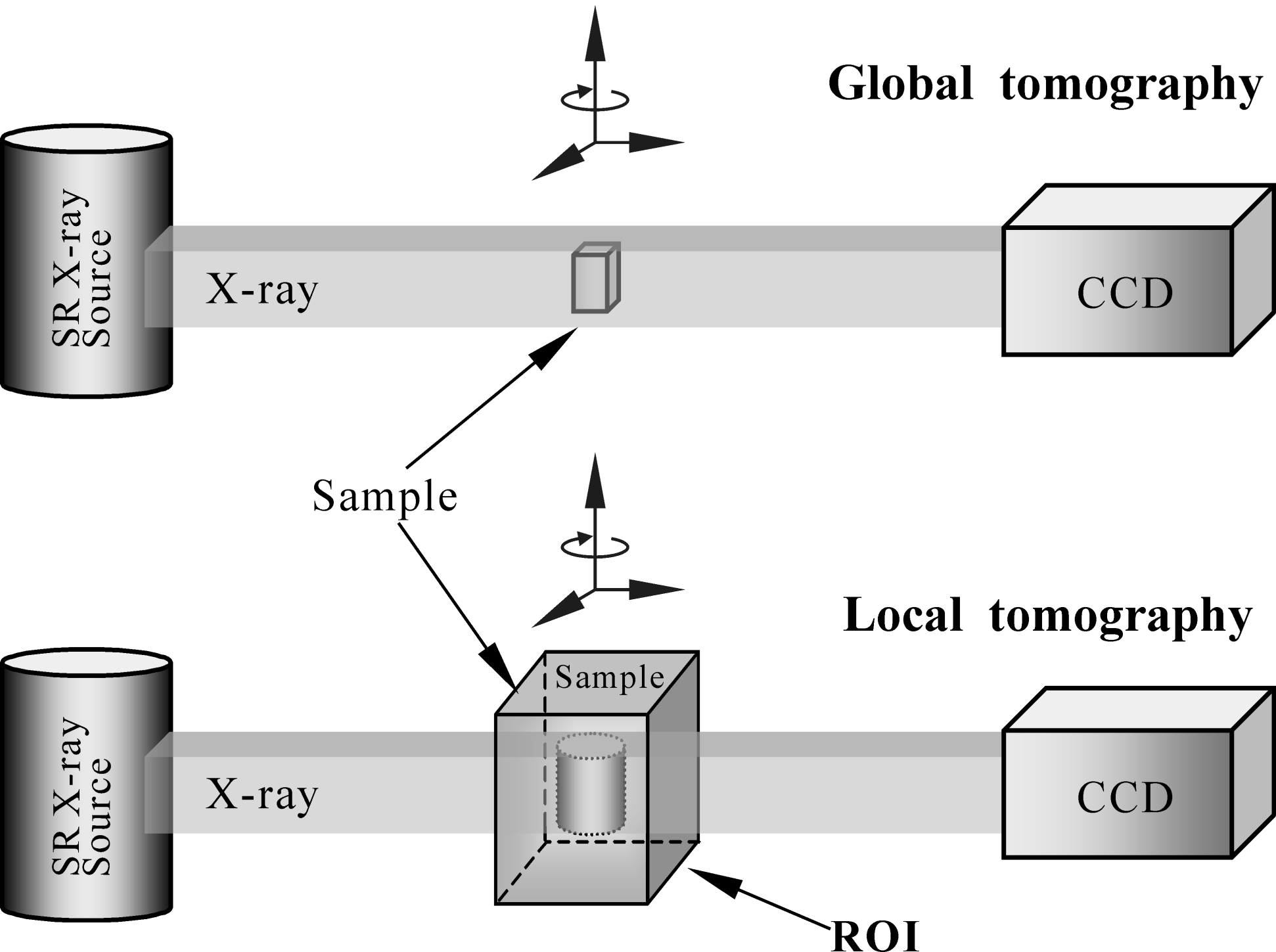
Global tomography
SR X-ray Source
X-ray
CCD
Sample
Local tomography
SR X-ray Source
Sample
X-ray
CCD
ROI

(a)

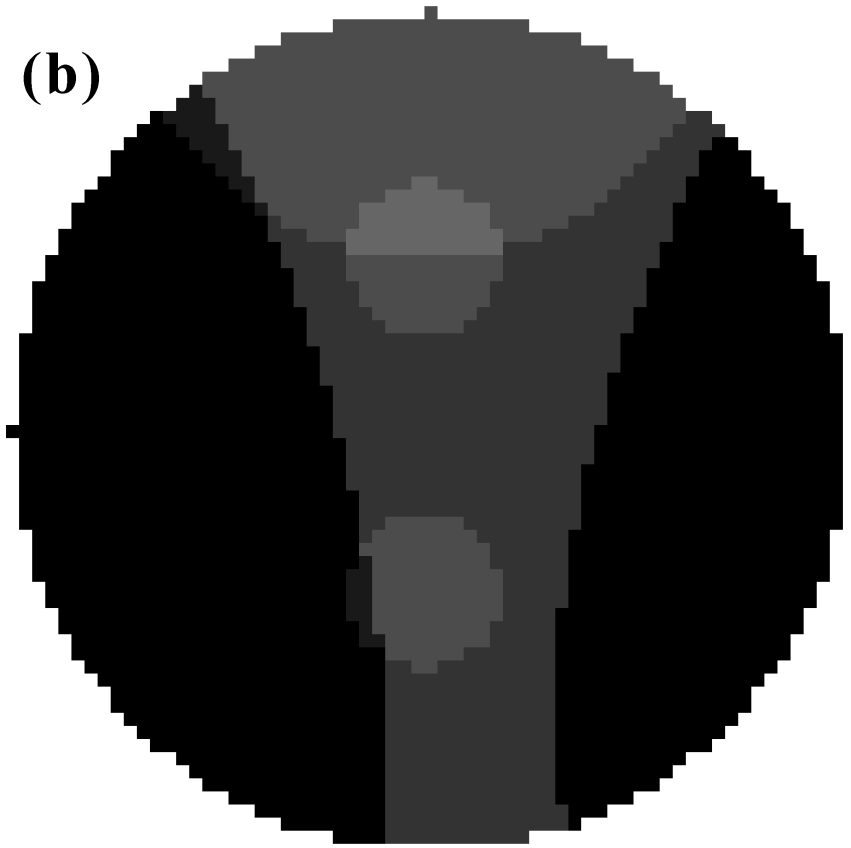
(b)

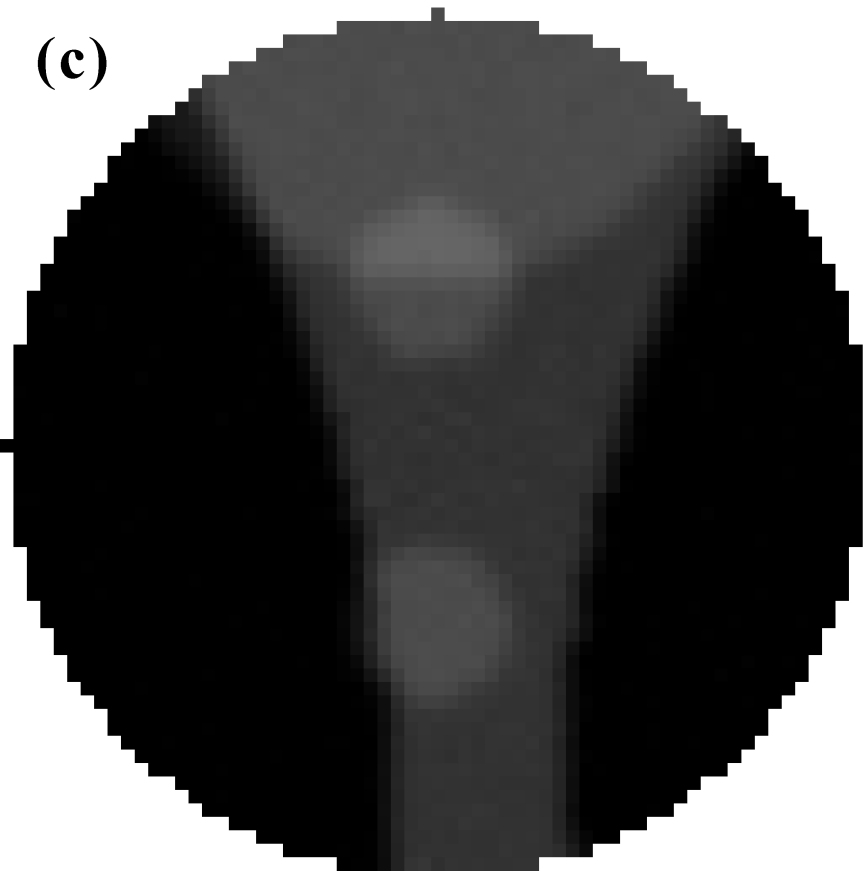
(c)

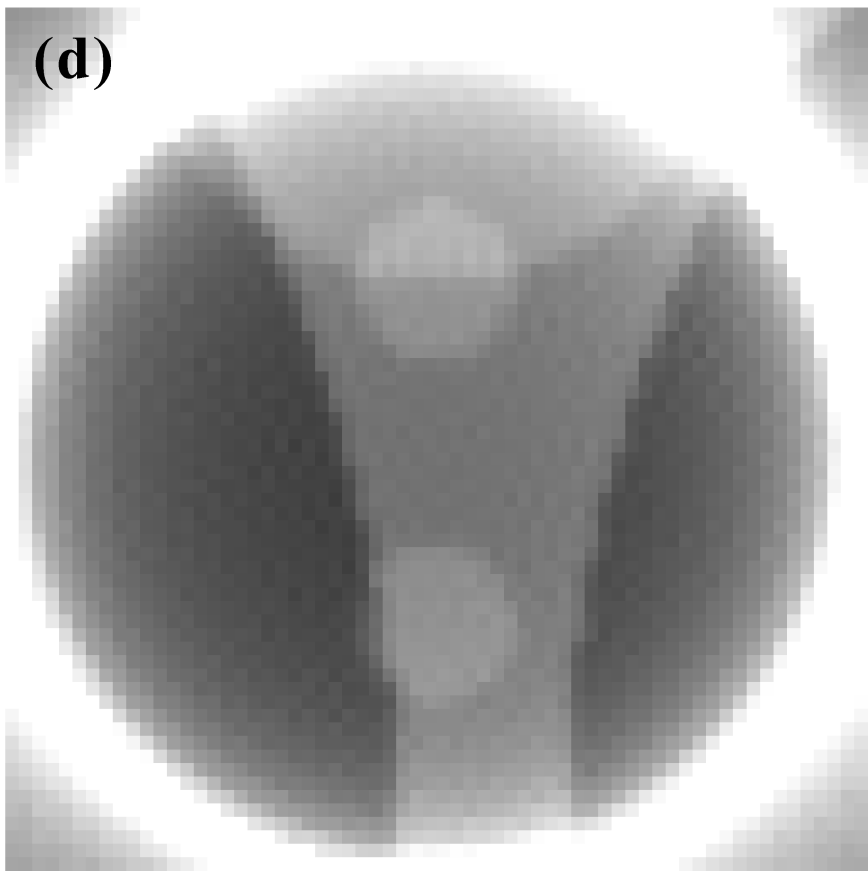
(d)

3

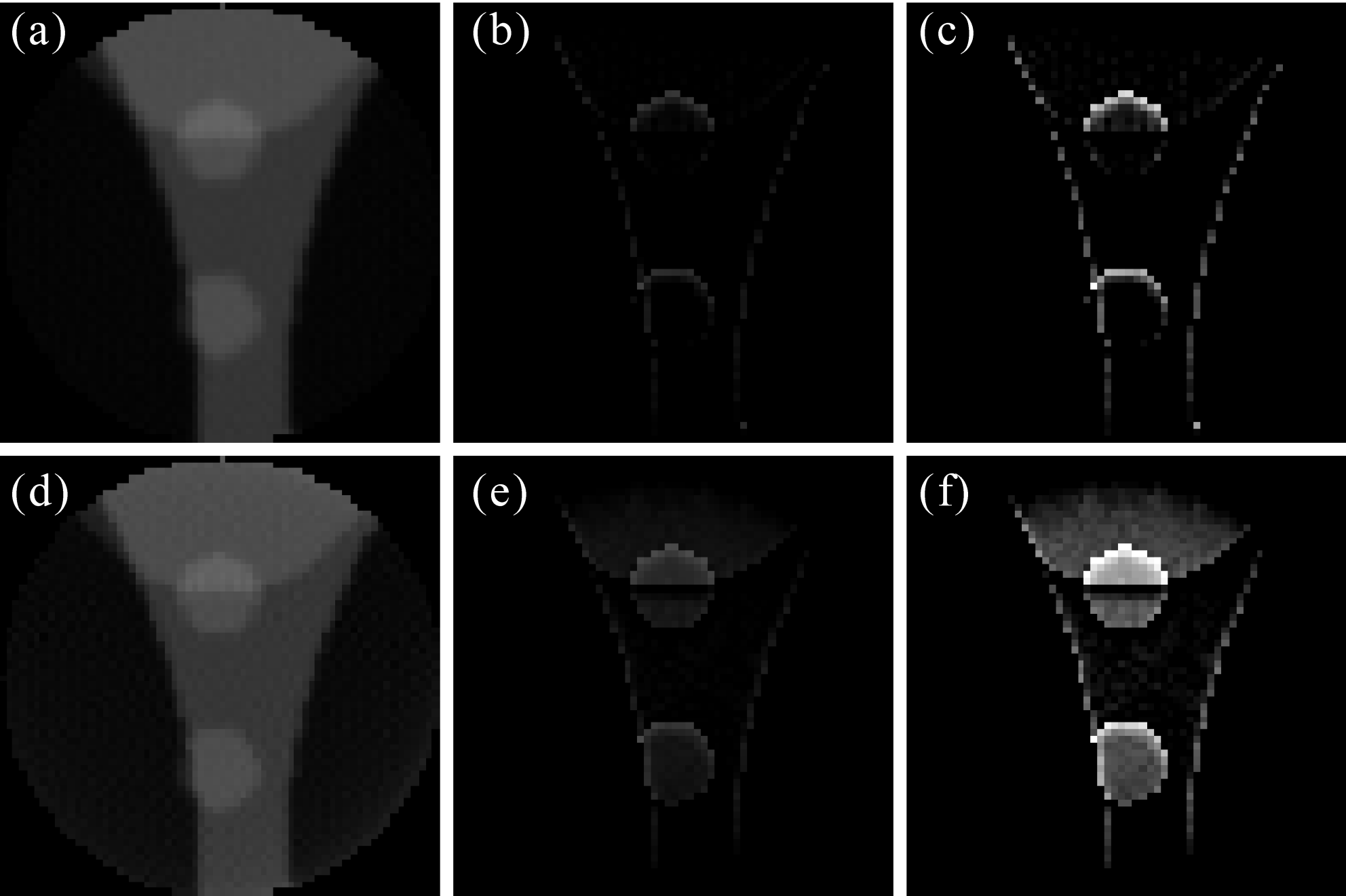

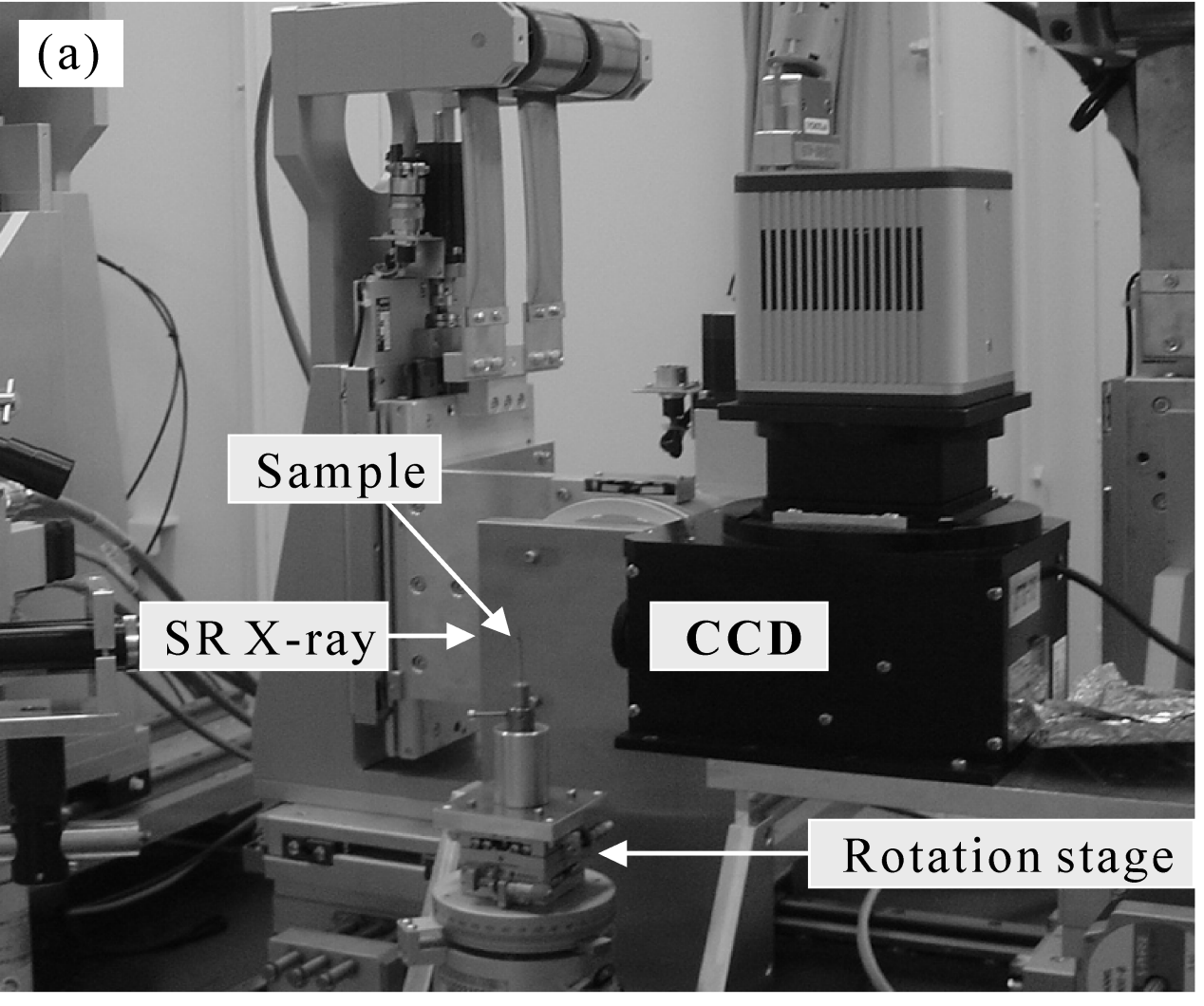
(a)
Sample
SR X-ray
CCD
Rotation stage

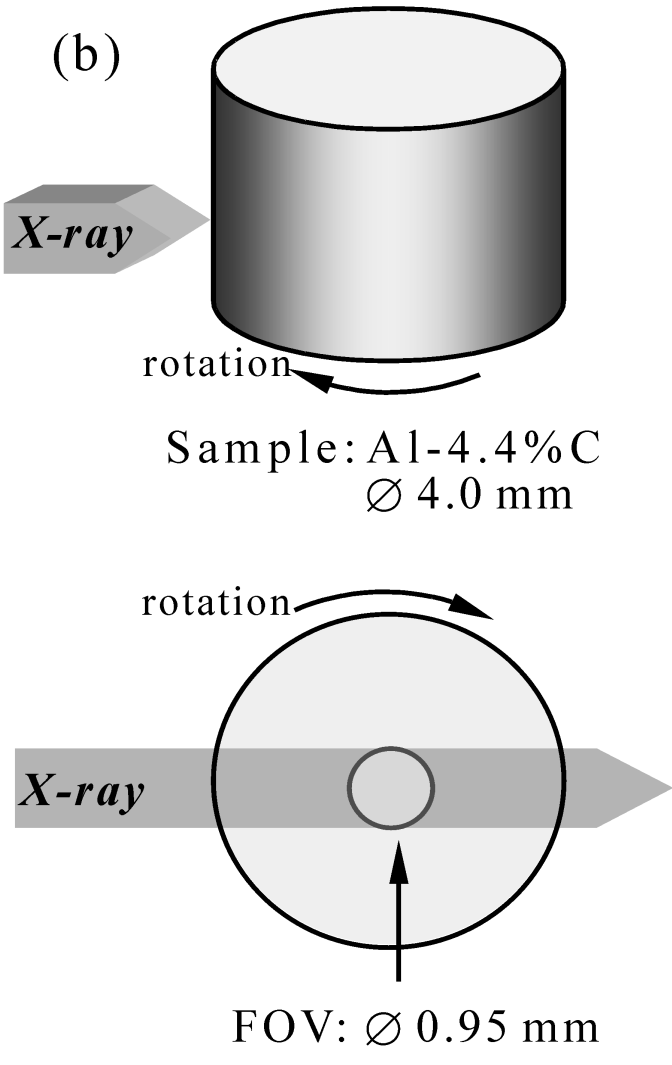
(b)
X-ray
rotation
Sample: Al-4.4%C
∅ 4.0 mm
rotation
X-ray
FOV: ∅ 0.95 mm

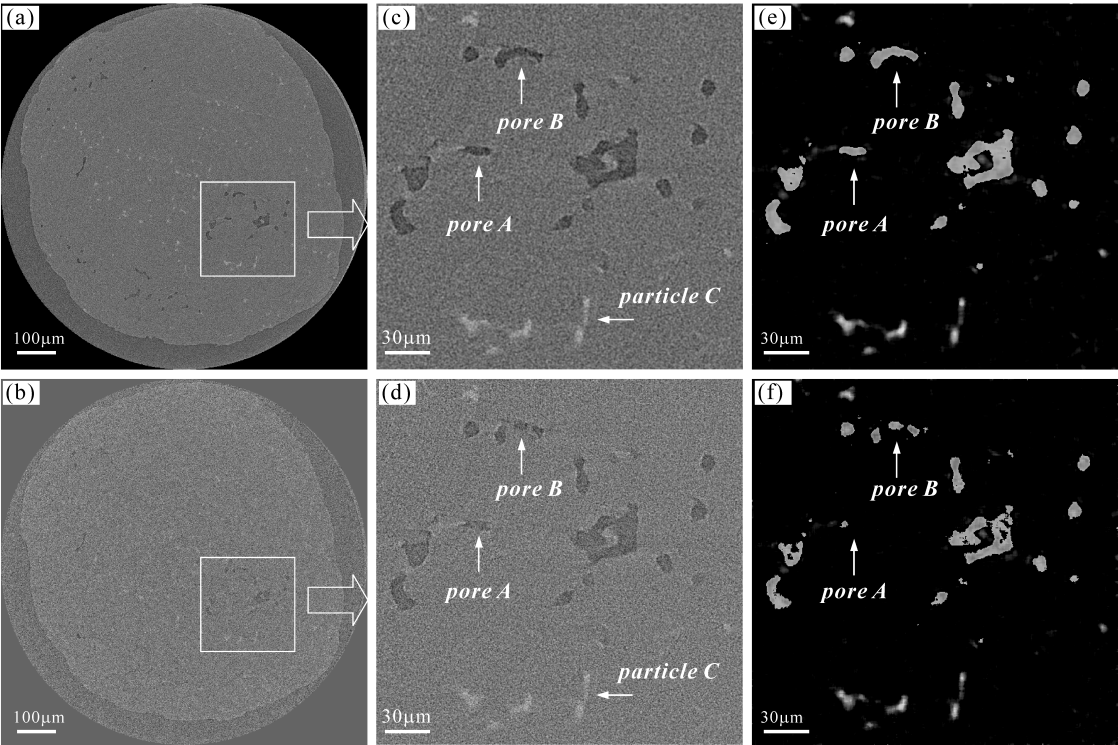
(a)
100μm
(c)
pore B
pore A
particle C
30μm
(e)
pore B
pore A
30μm
(b)
100μm
(d)
pore B
pore A
particle C
30μm
(f)
pore B
pore A
30μm

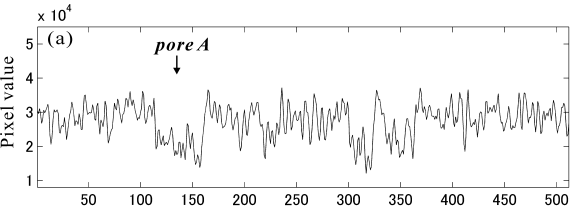
x 10^4
(a)
pore A
Pixel value
5
4
3
2
1
50
100
150
200
250
300
350
400
450
500

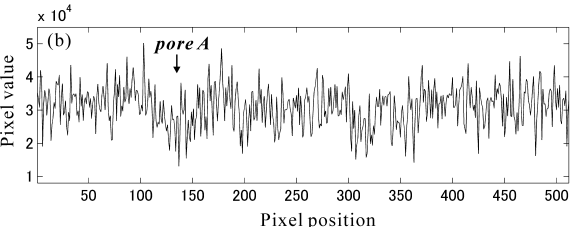
x 10^4
(b)
pore A
Pixel value
5
4
3
2
1
50
100
150
200
250
300
350
400
450
500
Pixel position

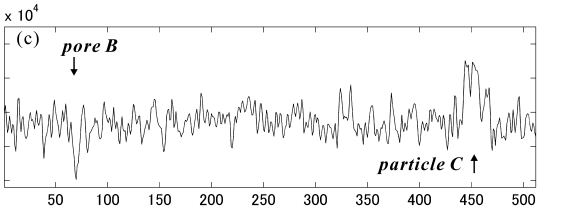
x 10^4
(c)
pore B
particle C
5
4
3
2
1
50
100
150
200
250
300
350
400
450
500

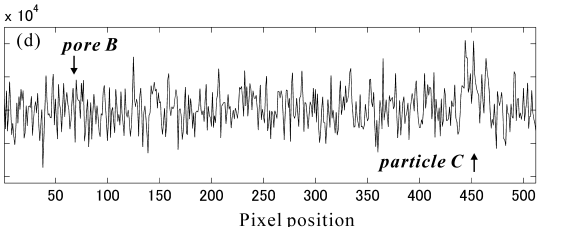
x 10^4
(d)
pore B
particle C
5
4
3
2
1
50
100
150
200
250
300
350
400
450
500
Pixel position

7

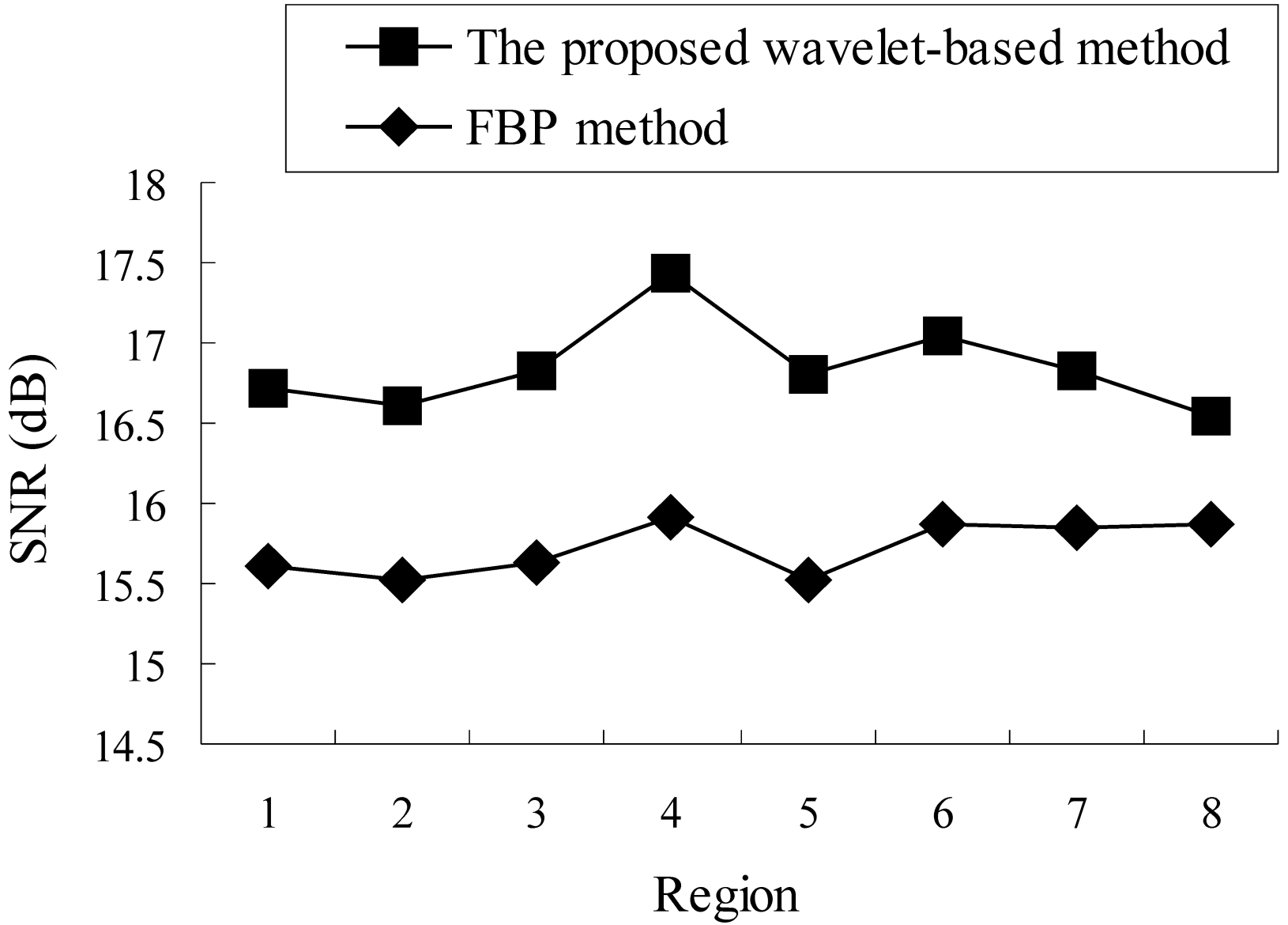
The proposed wavelet-based method
FBP method
SNR (dB)
18
17.5
17
16.5
16
15.5
15
14.5
1
2
3
4
5
6
7
8
Region

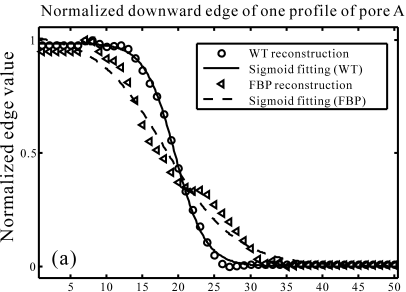
Normalized downward edge of one profile of pore A
Normalized edge value
WT reconstruction
Sigmoid fitting (WT)
FBP reconstruction
Sigmoid fitting (FBP)
(a)

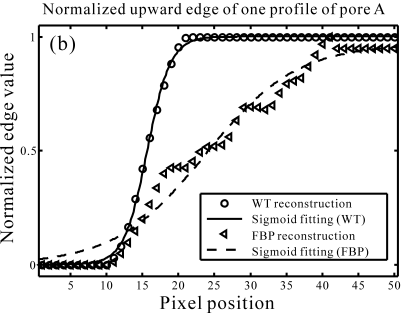
Normalized upward edge of one profile of pore A
Normalized edge value
(b)
WT reconstruction
Sigmoid fitting (WT)
FBP reconstruction
Sigmoid fitting (FBP)
Pixel position

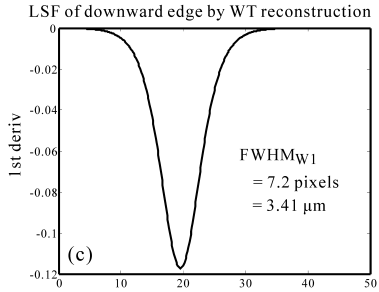
LSF of downward edge by WT reconstruction
1st deriv
FWHM$_{W1}$
= 7.2 pixels
= 3.41 μm
(c)

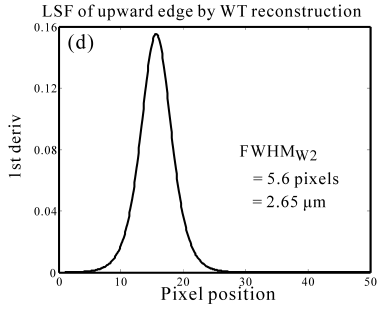
LSF of upward edge by WT reconstruction
1st deriv
FWHM$_{W2}$
= 5.6 pixels
= 2.65 μm
(d)
Pixel position

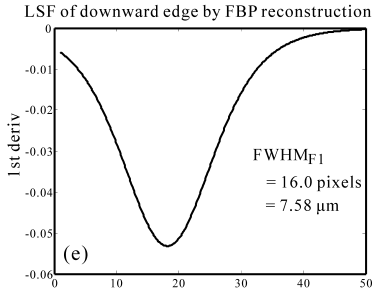
LSF of downward edge by FBP reconstruction
1st deriv
FWHM$_{F1}$
= 16.0 pixels
= 7.58 μm
(e)

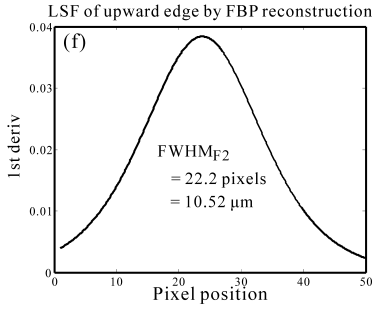
LSF of upward edge by FBP reconstruction
1st deriv
FWHM$_{F2}$
= 22.2 pixels
= 10.52 μm
(f)
Pixel position

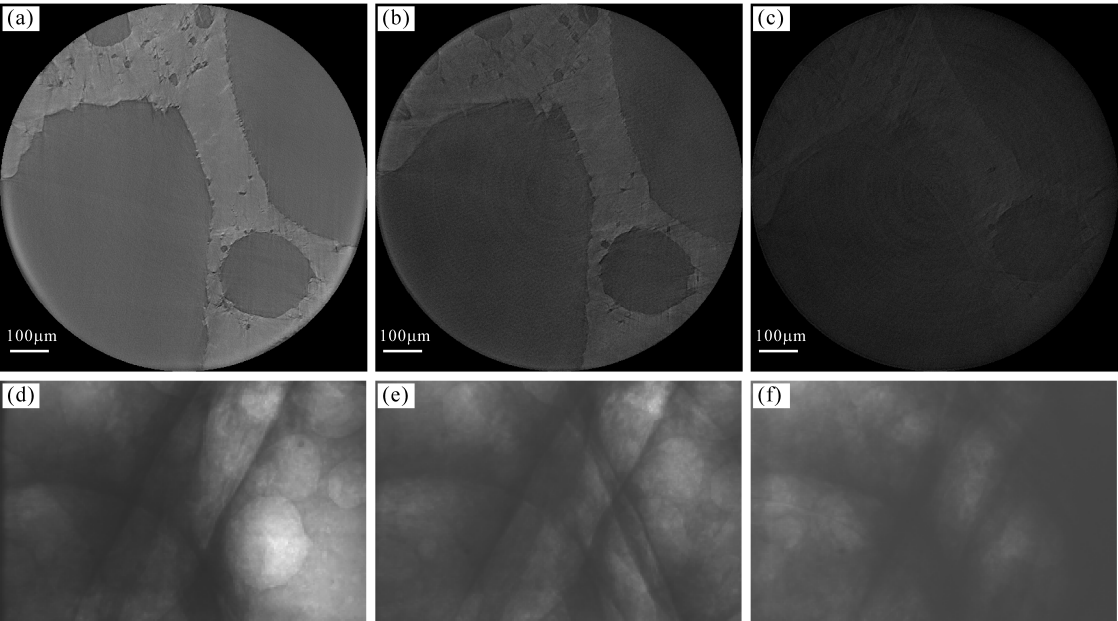
(a)
100μm
(b)
100μm
(c)
100μm
(d)
(e)
(f)